Acta Polytechnica **66**(4):375–385, 2026
https://doi.org/10.14311/AP.2026.66.0375
© 2026 The Author(s). Licensed under a CC-BY 4.0 licence
Published by the Czech Technical University in Prague

FREQUENCY AND PHASE TRACKING FOR EXCITATION CAPACITOR FAULT DETECTION IN A SELF-EXCITED INDUCTION GENERATOR USING THE ZCT METHOD

Ali Dilmi[a,*], Ahcene Bouzida[a], Nacera Yassa[a], Belynda Fares[b]

[a] *University of Bouira, Faculty of Applied Sciences, Materials, and Sustainable Development Laboratory (LMDD), 10000 Bouira, Algeria*

[b] *Université de Bejaia, Faculté de Technologie, Laboratoire de Technologie Industrielle et de l'Information LTII, 06000 Bejaia, Algeria*

[*] corresponding author: ali.dilmi@univ-bouira.dz

Abstract. This paper presents a methodology for detecting excitation capacitor faults in self-excited induction generators (SEIGs) used in wind energy systems operating in isolated or rural areas. The proposed approach combines frequency and phase tracking with zero-crossing time rate analysis for real-time anomaly detection. The SEIG is modelled using the finite element method (FEM) to simulate its electromechanical behaviour under various fault conditions. Fault scenarios are introduced by progressively disconnecting excitation capacitors connected in parallel and series, thus simulating failures ranging from one to five units. Monitoring zero-crossing intervals and phase variations enables accurate fault detection without relying on computationally intensive spectral techniques. The results confirm the effectiveness of the proposed methodology in identifying fault-induced distortions and improving the reliability of SEIG-based wind energy systems.

Keywords: Wind energy, self-excitation generator, diagnostic, finite elements method, zero-crossing time rate.

1. Introduction

The escalating threat posed by greenhouse gas emissions has intensified global efforts to transition towards renewable energy sources [1]. Among these, wind energy has emerged as a clean, abundant, and sustainable resource with significant potential for power generation and minimal environmental impact [2].

Self-excited induction generators (SEIGs) are particularly well suited for wind energy applications in remote and isolated areas due to their ability to operate without an external excitation source. They offer several advantages, including cost-effectiveness, low maintenance requirements, robust construction, and a brushless squirrel-cage rotor [3]. In addition, their nonlinear voltage-speed for characteristic, governed by magnetic saturation, allows stable operation even under slight deviations from the rated speed [4].

The operational principle of SEIGs involves connecting excitation capacitors to the stator terminals and driving the machine with a prime mover [5]. Under the appropriate conditions, the generator achieves self-excitation, resulting in a steady state in which the voltage and current oscillate at a stable amplitude and frequency [6]. However, the deployment of SEIGs in off-grid wind energy systems necessitates continuous monitoring to detect faults at an early stage and thereby preventing catastrophic failures. While previous studies have investigated rotor cage faults and stator imbalances [7], this work specifically addresses faults in excitation capacitors, which can severely affect system performance.

Capacitor faults disrupt the generator's excitation balance, leading to distorted stator currents, erratic torque fluctuations, and voltage instability, which may ultimately result in total system failure. Although the minimum and maximum capacitance requirements for self-excitation are well established, selecting excessively high capacitance values is neither economically nor technically justified [8]. In order to investigate these effects, this study employed the time-stepping finite element method (TSFEM) to accurately model SEIG dynamics under fault conditions [9].

Traditional fault diagnosis techniques, such as those based on equivalent series resistance (ESR), have been applied [10], primarily focusing on gradual degradation through drift modelling. However, these approaches rely on oversimplified representations of the complex physical processes underlying the capacitor deterioration. Open-capacitor faults in SEIGs have been reported to reduce the generated torque to zero and destabilise the system. The Hilbert-Huang Transform (HHT) has also been used for fault detection in a previous study [11]. Nevertheless, the progressive aging of capacitors and its incremental impact on system performance were not addressed in that study.

To address these limitations, we developed and implemented a finite element method (FEM) simulation alongside a zero-crossing-based technique for real-time tracking of instantaneous frequency and phase shifts in stator currents [12, 13]. This approach provides a computationally efficient and reliable method for

detecting capacitor faults by analysing deviations in zero-crossing intervals and phase alignment. By eliminating the need for complex spectral decomposition, the proposed technique enhances detection accuracy and reduces computational overhead [14]. Its effectiveness has been validated through experiments on SEIGs under both healthy and faulty conditions, simulating a progressive degradation of capacitors [15].

The remainder of the paper is organised as follows. Section 2 presents the SEIG mathematical model using TSFEM. Section 3 describes the excitation capacitor fault scenarios. Section 4 covers the theoretical background of zero-crossing rate (ZCR) estimation. Section 5 presents the simulation results and analysis. Section 6 outlines the data acquisition process, while Section 7 details the zero-crossing detection methodology and experimental results. Section 8 concludes the paper and discusses possible directions for future research.

2. Finite element modelling of SEIG

In an SEIG-based wind energy system, the rotor, driven by a wind turbine, induces voltage across the capacitors connected to the stator terminals. This voltage defines the terminal voltage of the generator. Figure 1 shows the system scheme.

The FEM is employed to evaluate the electromagnetic behaviour of the generator under varying operating conditions. FEM models the magnetic circuit geometry, stator winding and rotor bar arrangements, air-gap slotting, and the nonlinear properties of ferromagnetic materials. The motion of the rotor is coupled with the field equations, as expressed by the two-dimensional Equation (1) [16]:

$$\nabla \times v\Delta \times \overrightarrow{A} = \overrightarrow{J_0}, \tag{1}$$

where $\vec{A}$ is the magnetic vector potential, $\overrightarrow{J_0}$ is the current density in z-axis, and V is the reluctivity.

The circuit and field equations are coupled to compute the total current of each conductor. The resulting current is given by:

$$\overrightarrow{J_0} = -\delta\frac{\partial \vec{A}}{\partial t} - \delta\frac{\Delta V}{l}, \tag{2}$$

where ΔV is the potential difference along the conductor, δ is the electrical conductivity, t is time, and l is the conductor length.

The corresponding current is given by Equation (3) [16]:

$$i = -\iint \delta\left(\frac{\partial A}{\partial t} + \Delta V\right) dS. \tag{3}$$

Equation (4) represents a general circuit, expressed in a matrix form, consisting of a voltage supply E, resistance R, and inductance L:

$$[E] = [R][i] + [L]\frac{di}{dt}. \tag{4}$$

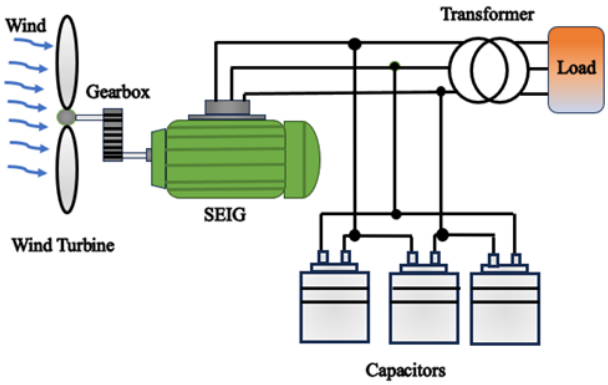

Figure 1. SEIG in wind system.

The general finite element (FE) matrix equation is derived using the standard Galerkin method, as presented in Equation (5):

$$\begin{bmatrix} G & H & 0 \\ 0 & W & D \\ 0 & D^T & -Z \end{bmatrix} \begin{bmatrix} A \\ \Delta V \\ i \end{bmatrix} + \begin{bmatrix} Q & 0 & 0 \\ H^T & 0 & 0 \\ 0 & 0 & -L_0 \end{bmatrix} \frac{\partial}{\partial t} \begin{bmatrix} A \\ \Delta V \\ i \end{bmatrix} = \begin{bmatrix} J_0 \\ 0 \\ -xE \end{bmatrix}, \tag{5}$$

where:

$$G_{ij} = \int v\nabla N_i \nabla N_j dS, \tag{6}$$

$$H_{ij} = \int \sigma N_i dS, \tag{7}$$

$$W_{kk} = \int_k \sigma ds, \tag{8}$$

$$L_0 = \int J_0 N_i ds. \tag{9}$$

Integrations of G, Q, and J are carried out over the entire model, whereas for W and H, they are performed over conductor K. R and L are diagonal matrices representing resistances and inductances, respectively. D is a sparse matrix, with entries of $+1$ and -1 indicating the direction of the current flow in a conductor [17].

Accurately assessing the minimum capacitance required for self-excitation of an induction generator is of considerable practical significance. Numerous numerical methods for determining the required excitation capacitance have been investigated in previous studies [18]. In this work, the precise values of the minimum capacitance for self-excitation are derived based on Equation (10) [19]:

$$C_{\Delta\,\min} = \frac{Q_g}{3 \times v^2 \times 2 \times \pi \times f}, \tag{10}$$

where Q_g denotes the reactive power consumed during generator operation, and v represents the single-phase voltage.

The required capacitance C_Δ is determined by evaluating the reactive power consumed by the SEIG.

Various equations can be applied to compute this parameter accurately [20].

$$P_n = S\cos\varphi_m\eta_m, \tag{11}$$

$$Q_m = S \times \sin\varphi_m, \tag{12}$$

$$S = \sqrt{3} \times U_{\text{line}} \times I_{\text{line}}. \tag{13}$$

The electrical power output of the induction machine in generator mode is given by Equation (14):

$$P_{\text{elg}} = \frac{P_n}{\eta_m} \times \frac{\sin\varphi_g}{\sin\varphi_m}. \tag{14}$$

For induction machines, power equivalence between the motor and generator modes must be maintained. This requirement is expressed mathematically in Equation (15):

$$S_{\text{motor}} = S_{\text{generator}}, \tag{15}$$

where S denotes the apparent power in each mode.

This relationship ensures that the electrical power generated in generator mode matches the power consumed during motor operation. The generator-mode electrical power is given by Equation (16) [21]:

$$Q_m = \frac{P_n}{\eta_m}\tan\varphi_m. \tag{16}$$

Following the evaluation of reactive energy in the motor mode, the reactive power in generator mode is computed as shown in Equation (17):

$$Q_g = \frac{\sin\varphi_g}{\sin\varphi_m} \times Q_m. \tag{17}$$

In this context, P_n denotes the mechanical power at a rated capacity, η_m the efficiency of the driving mechanism, and φ_m the power factor angle during the motor operation.

A finite element model of a 4.087 MW, two-pole squirrel-cage SEIG with a rated RMS voltage of 3 000 V was developed in Ansys Maxwell 2D based on the machine's design specifications. The computational domain was discretised with approximately 85 000 quadratic finite elements, with additional refinement in critical regions, particularly the air gap, to improve numerical accuracy. Magnetic boundary conditions were imposed to accurately represent the field distribution and reduce numerical errors.

Transient simulations were conducted over 5 s to capture the generator startup dynamics. The Backward Euler scheme was employed for time integration using the General Transient solver, whith a nonlinear convergence tolerance was set to 10^{-4}. An adaptive time-stepping strategy, with steps ranging from 0.001 s to 1 s, ensured both numerical stability and computational efficiency. The main SEIG parameters are listed in Table 1, while Figure 2 illustrates the magnetic field distribution obtained from the finite element (FE) analysis.

Figures 3, 4, and 5 present the dynamic performance of the SEIG during self-starting, as captured by the validated FEM model. The rotor was maintained at a constant speed n, and the plots were generated from the stored simulation data. Figures 6 and 7 show the startup voltage and current responses.

Figure 5 shows the torque curve, which drops rapidly at first before stabilising. This behaviour is typical of a generator adapting to its load during a startup.

The system exhibits balanced voltage across all phases with no significant fluctuations, indicating

Parameter	Values
Rated Power	4.087 MW
Rated Voltage	3 000 V
Coupling Method	Wye
Number of Poles	2
Rated Speed	3 135 rpm
Rated Frequency	51.83 Hz
Operating Temperature	75 °C

TABLE 1. Parameters of the (SEIG).

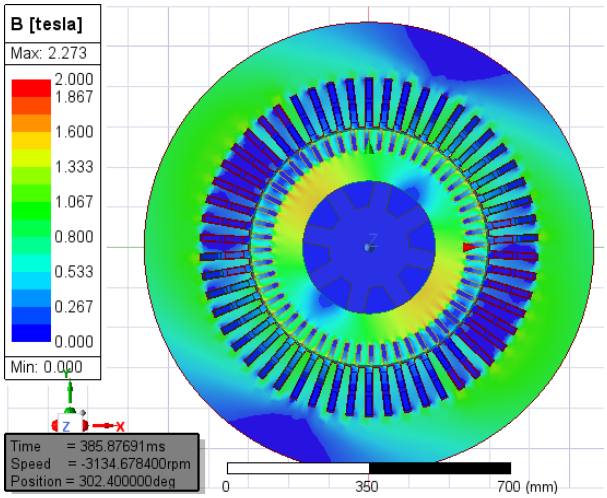

FIGURE 2. Representation of the field distribution using finite element (FE) analysis.

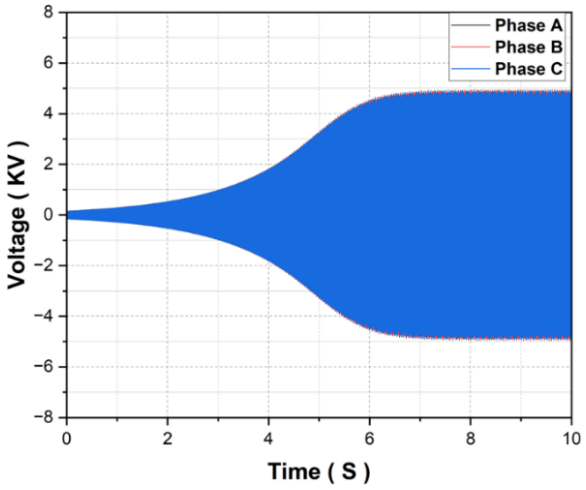

FIGURE 3. The process of voltage buildup for SEIG during excitation under no-load conditions.

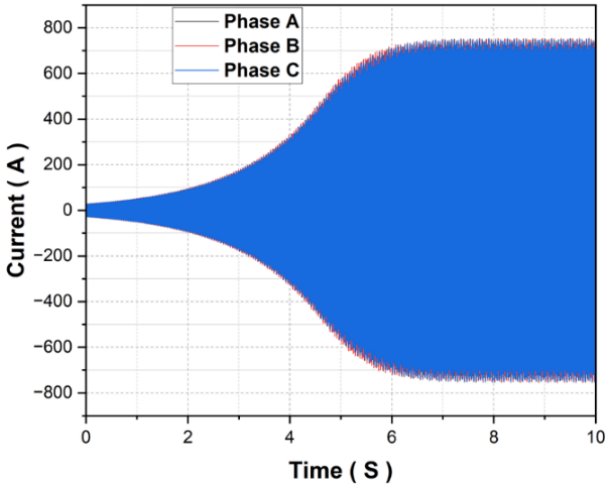

Figure 4. Line current behaviour of SEIG during the excitation process under no load conditions.

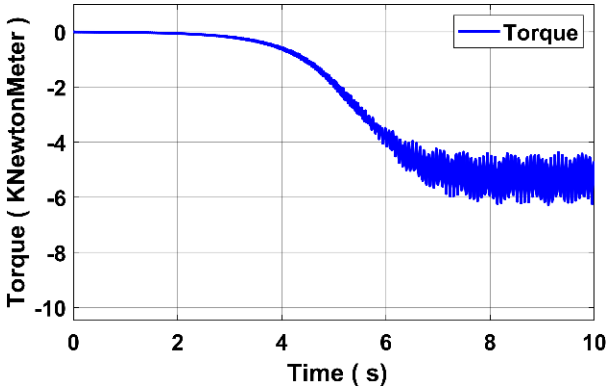

Figure 5. The electromagnetic torque characteristics of SEIG during the excitation process under no-load conditions.

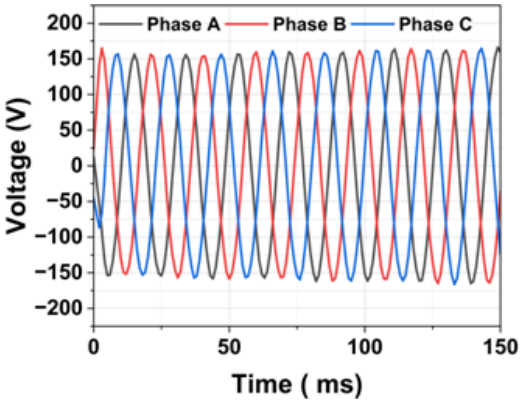

Figure 6. Startup voltage behaviour.

a stable generator operation. As shown in Figure 3, the voltage builds up progressively during the self-excitation stage, which lasts approximately 7 s. The voltage then stabilises at a peak value of about 424 V, corresponding to an RMS value of nearly 300 V, confirming that the generator reaches a stable nominal operating voltage.

The current waveforms of phases A, B, and C shown in Figure 4 exhibit smooth and symmetrical behaviour,

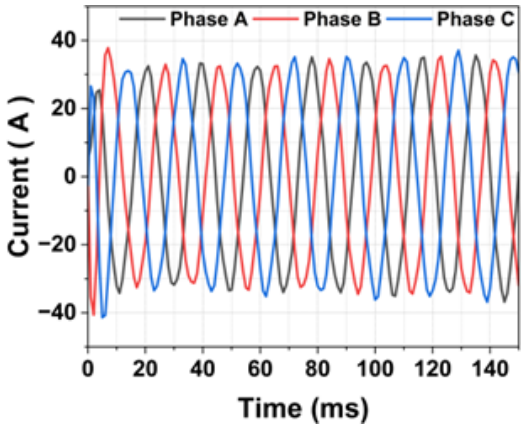

Figure 7. Startup current behaviour.

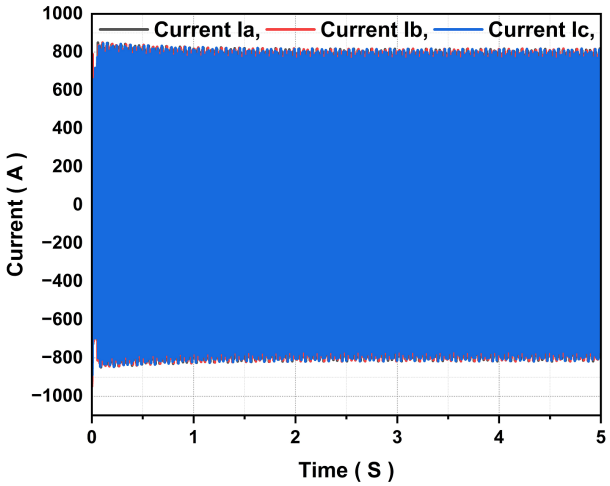

Figure 8. Current under load conditions.

indicating a balanced three-phase operation. The currents increase gradually during the excitation phase as the magnetic field builds up inside the machine. Once a steady state is reached, the waveforms remain stable with no noticeable distortion or phase imbalance, which confirms a the healthy electromagnetic behaviour of the SEIG under no-load conditions.

The electromagnetic torque curve illustrated in Figure 5 shows the torque evolution during the self-excitation process. Initially, the torque remains close to zero due to the absence of electrical loading. As excitation progresses and the magnetic field builds up, the torque gradually becomes negative, indicating generator operation where mechanical power is converted into electrical power. After about 7 s, the torque stabilises at a constant negative value, confirming that electromagnetic steady-state conditions have been reached.

After reaching the steady-state current and voltage conditions, the generator is connected to a balanced 10 Ω load at $t = 0.05$ s. As shown in Figure 8, the current magnitude increases abruptly and stabilises at a peak value of approximately 800 A. In contrast, Figure 9 shows a gradual decrease in the phase voltage from its initial value until it reaches a steady peak

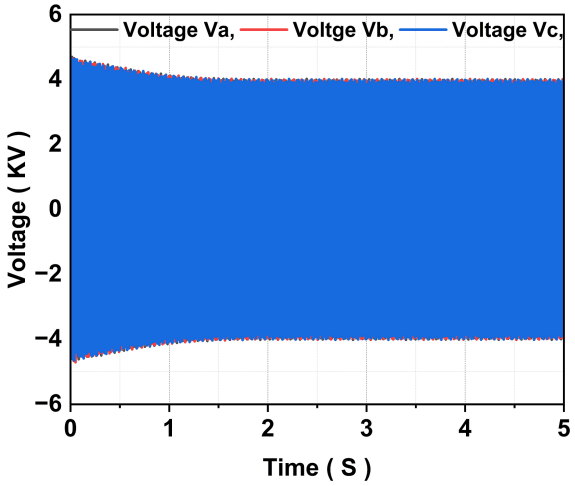

FIGURE 9. Voltage under load conditions.

value of about 4 kV (approximately 2.8 kV RMS). Regarding the mechanical behavior, Figure 10 indicates that the electromagnetic torque settles at a steady-state value of about −10 kNm. This response is attributed to the inherent characteristics of the SEIG, where an increase in the load current leads to an increase in the internal voltage drop, which causes the system to establish a new equilibrium between the input mechanical power and the electrical power delivered to the load.

3. FAULT SCENARIOS

To ensure stable self-excitation, the excitation capacitance was organised into multiple groups. Each branch comprises four series-connected capacitors sharing 3 600 V, and twenty-eight branches are connected in parallel to provide the required total capacitance, ensuring a balanced voltage distribution, and safe generator operation.

Progressive degradation was simulated by disconnecting capacitor elements in phase C, while phases A and B remained intact, which represents typical aging mechanisms, such as thermal cycling, overvoltage, partial discharges, and material deterioration. Six fault scenarios were defined in order to investigate varying levels of capacitor degradation. Figure 11 illustrates the main components of the excitation capacitors.

4. ZERO-CROSSING RATE (ZCR) ESTIMATION

The ZCR quantifies the number of times a signal crosses the zero-amplitude axis within a defined time window [22]. Each zero-crossing corresponds to a transition between positive and negative amplitudes, making ZCR effective for analysing periodic or quasi-periodic signals. It is particularly advantageous in high-noise environments, where spectral methods may be computationally expensive or sensitive to disturbances [23].

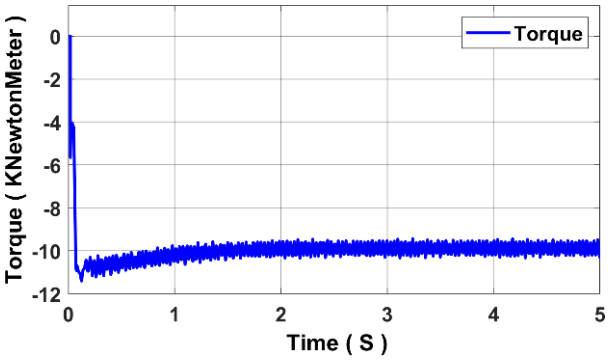

FIGURE 10. The electromagnetic torque characteristics of SEIG during the excitation process under load conditions.

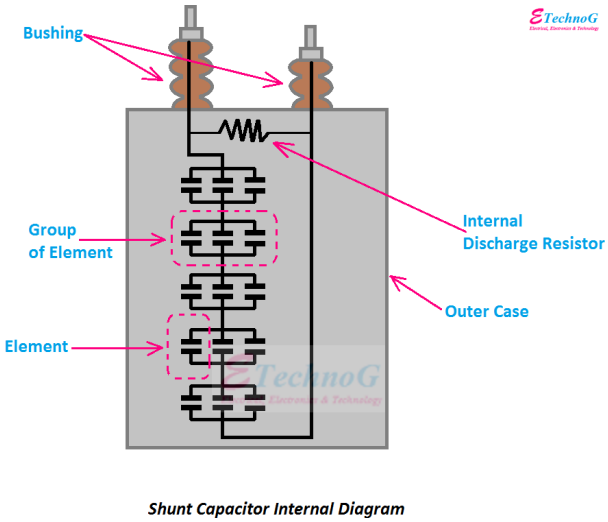

FIGURE 11. Shunt capacitor internal diagram.

In electrical signal analysis, the ZCR provides a computationally efficient method for estimating instantaneous frequency in AC waveforms, such as current or voltage in electric machines. Variations in frequency directly impact the rate of zero-crossings, enabling real-time tracking [24].

ZCR can also reveal phase information when applied across multiple channels or combined with other signal processing techniques [25]. This makes it suitable for fault detection, including identifying asymmetries in stator currents caused by capacitor degradation in SEIGs, which alters waveform periodicity and zero-crossing patterns, without requiring a full spectral decomposition.

For a discrete-time signal $x[n]$, the ZCR over a window of length N is given by Equation (18) [26]:

$$\mathrm{ZCR} = \frac{1}{2N}\sum_{n=1}^{N} |\operatorname{sgn}(x[n]) - \operatorname{sgn}(x[n-1])|. \quad (18)$$

The sign function sgn is defined as follows [27]:

$$\operatorname{sgn}(x) = \begin{cases} 1, & x > 0 \\ 0, & x = 0 \\ -1. & x < 0 \end{cases} \quad (19)$$

Each zero-crossing corresponds approximately to half a period of a sinusoidal signal [28]. Therefore, an approximate frequency estimate, f_{ZCR} in Hz, assuming a sampling rate f_s, is given by Equation (20):

$$f_{\text{ZCR}} = \frac{\text{ZCR} \cdot f_s}{2}. \tag{20}$$

4.1. Instantaneous frequency

Instantaneous frequency provides a time-varying measure of the frequency content of a signal, especially useful for non-stationary signals. For a real-valued signal $x(t)x(t)$, the instantaneous frequency $f(t)f(t)$ can be derived from its analytic signal.

Let the analytic signal $z(t)$ of $x(t)$ be:

$$Z(t) = x(t) + j \cdot \hat{x}(t), \tag{21}$$

where $\hat{x}(t)$ is the Hilbert transform of $x(t)$. The instantaneous phase $\phi(t)$ is:

$$\phi(t) = \arg(Z(t)) = \tan^{-1}\left(\frac{\hat{x}(t)}{x(t)}\right). \tag{22}$$

Then, the instantaneous frequency $f(t)$ is:

$$25f(t) = \frac{1}{2\pi}\frac{d\phi(t)}{dt}. \tag{23}$$

In discrete time, for samples $x[n]$, the instantaneous frequency can be approximated as:

$$f[n] = \frac{f_s}{2\pi}(\phi[n] - \phi[n-1]), \tag{24}$$

where f_s is the sampling frequency and $\phi[n]$ is the phase at sample N [29].

4.2. Phase differences between three-phase currents

Let $i_a(t), i_b(t), i_c(t)$ be the three-phase currents. Their phase difference can be estimated using the instantaneous phase of each signal.

Compute the analytic signals for each current:

$$\begin{cases} Z_a(t) = i_a(t) + j \times \widehat{i_a}(t), \\ Z_b(t) = i_b(t) + j \times \widehat{i_b}(t), \\ Z_c(t) = i_c(t) + j \times \widehat{i_c}(t). \end{cases} \tag{25}$$

Extract the instantaneous phases:

$$\begin{cases} f_a(t) = \arg(Z_a(t)), \\ f_b(t) = \arg(Z_b(t)), \\ f_c(t) = \arg(Z_c(t)). \end{cases} \tag{26}$$

Compute the phase differences:

$$\begin{cases} \Delta f_{ab}(t) = f_a(t) - f_b(t), \\ \Delta f_{bc}(t) = f_b(t) - f_c(t), \\ \Delta f_{ca}(t) = f_c(t) - f_a(t). \end{cases} \tag{27}$$

These differences reveal the symmetry and distortion of the three-phase system. A sampling frequency of $f_s = 10\,\text{kHz}$ was used to achieve a high-resolution zero-crossing detection. A sliding window of $N = 1\,000$ samples (five cycles at 50 Hz) with 75 % overlap enabled smooth tracking of transitions and real-time frequency monitoring.

To preserve signal integrity, only DC offset removal was applied, with no additional digital filtering. The sliding-window averaging minimises noise sensitivity, providing robust performance under load variations while maintaining steady-state frequency deviations below 0.02 Hz.

5. Simulation results

5.1. Signal testing process using the ZCR

The testing process evaluates the effect of progressively increasing capacitor faults in phase C on the generated stator current, and how these effects can be detected using the ZCR by tracking the instantaneous frequency and phase shifts. The methodology involves the following steps:

6. Data acquisition

- The SEIG is configured with multiple excitation capacitors connected in parallel per phase to achieve the necessary value.
- Fault conditions are simulated by selectively removing 1 to 5 capacitors in phase C only, while phases A and B remain fully functional.
- For each fault level (from 1 capacitor missing to up to 5 capacitors), the three-phase stator current is recorded under identical load and operating conditions.

7. Zero-crossing detection

- The algorithm scans the phase C current signal for sign changes for each transition from positive to negative values and vice versa.
- Each sign change corresponds to a zero-crossing point, and its time-step is recorded.
- The ZCR is computed as the number of zero-crossings per unit of time, which is directly related to the instantaneous frequency of the waveform.

The ZCR is plotted in Figure 12.

Figure 12 shows the ZCR of the three-phase currents (i_a, i_b, i_c) over time. The crossing rates fluctuate between approximately $100\,\text{s}^{-1}$ and $110\,\text{s}^{-1}$, indicating slight variations in the system. Ideally, in a stable three-phase system, the frequency should remain close to the nominal value.

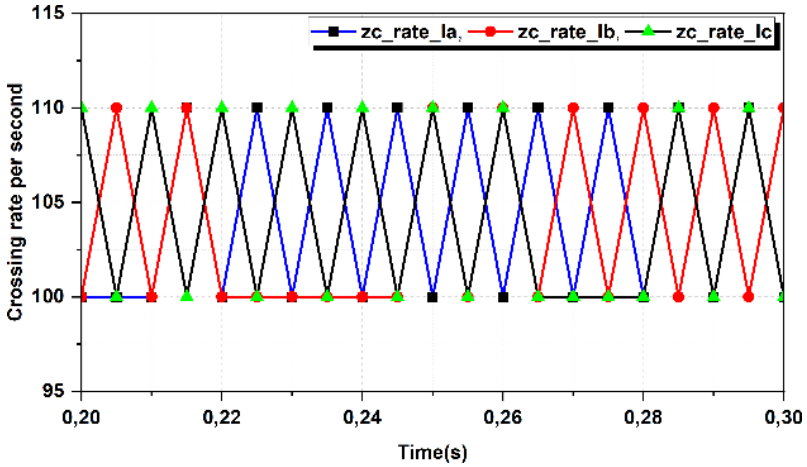

FIGURE 12. Zero-crossing rate per second for three-phase currents.

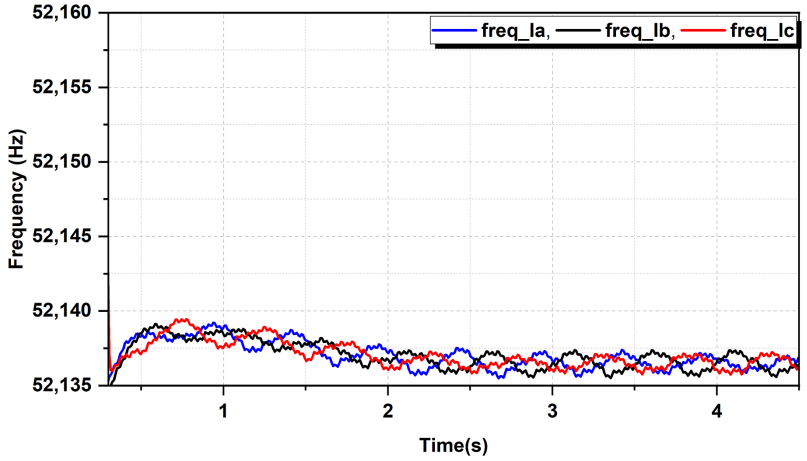

FIGURE 13. Estimated frequency of three-phase currents.

7.1. FREQUENCY STABILITY AND NOMINAL VALUE

Figures 13–18 show the estimated frequencies of the three-phase currents (i_a, i_b, i_c) for an induction generator with symmetric excitation capacitors.

The frequencies of all three phases are tightly clustered between 52.135 Hz and 52.160 Hz, indicating a stable and well-balanced system.

Figure 13 shows that the frequency and phase symmetry are stabble, which indicates that the generator and its excitation capacitorsare operating normally. Although minor variations remain within acceptable limits, continuous monitoring is recommended for early fault detection.

The results indicate that the progressively disconnecting the excitation capacitors in phase C significantly disturbs the temporal behaviour of the stator current, producing increasingly irregular ZCR patterns. These variations are consistently detected by the proposed algorithm, enabling early identification and grading of capacitor faults. Quantitative indicators were established to differentiate healthy and faulty conditions. Under normal operation, the generator frequency remains stable within a range of 52.135–52.160 Hz, with a mean value of 52.14 Hz and a standard deviation $\sigma < 0.005$. A fault is detected when the frequency deviation exceeds 0.5 % of the nominal value. Compared with the Fast Fourier Transform (FFT), which requires $\mathcal{O}(N \log N)$ complexity and multi-cycle windows, the Zero-Crossing Time (ZCT) method operates with linear complexity $\mathcal{O}(N)$ and reduces the computational overhead by approximately 30 %, enabling frequency deviation detection within a half-cycle. These results confirm that the proposed approach is effective for fast and reliable fault diagnosis in real-time SEIG monitoring.

Figures 19–21 illustrate the phase differences between phase pairs A-B, B-C, and A-C.

The phase-difference analysis of the phase pairs (A-B, B-C, and A-C) provides clear evidence of the impact of excitation capacitor degradation on the operational stability of the SEIG. Under healthy conditions, the phase differences remain tightly clustered, indicating strong phase symmetry and stable electromagnetic behaviour. For the A-B pair (Figure 19), the values are within the range -15.99×10^{-3} to -15.95×10^{-3}, whereas capacitor faults introduce significant dispersion ranging approximately from -16.25×10^{-3} to 16.025×10^{-3}, reflecting a clear loss of phase balance. A similar trend is observed for the B-C pair

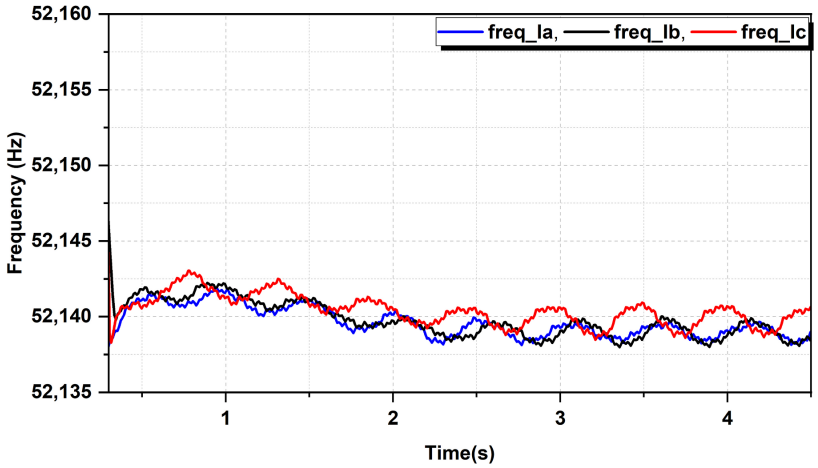

Figure 14. Estimated frequency of three-phase currents (I_a, I_b, I_c) for one capacitor failure.

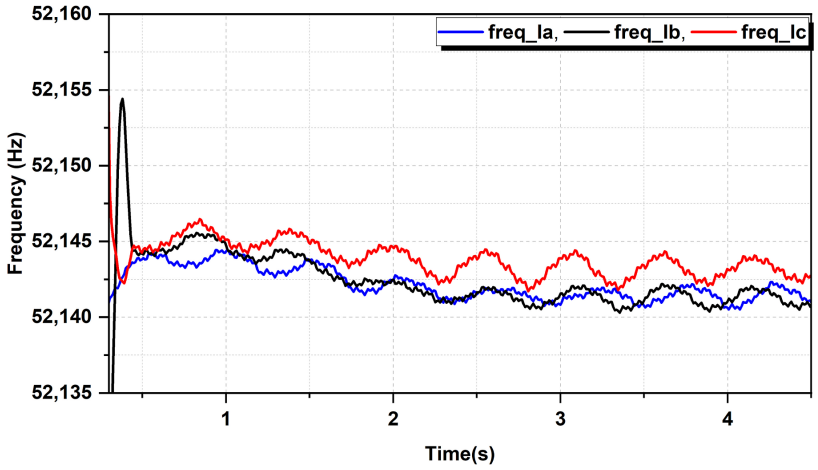

Figure 15. Estimated frequency of three-phase currents (I_a, I_b, I_c) for two capacitor failures.

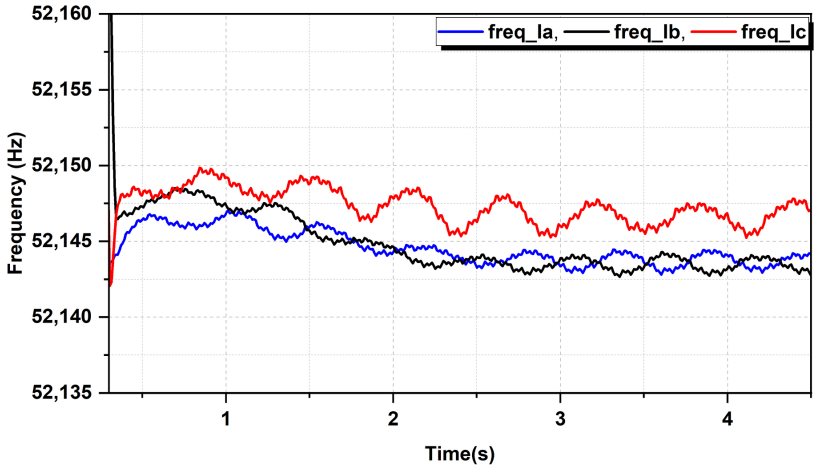

Figure 16. Estimated frequency of three-phase currents (I_a, I_b, I_c) for three capacitor failures.

(Figure 20), which exhibits stable values between -3.3×10^{-3} and -3.1×10^{-3} under normal operation, but becomes highly irregular under fault conditions.

This increased sensitivity, particularly in the case of the B-C pair, is physically rooted in the direct alteration of the system's nodal admittance matrix caused by the capacitance reduction, which triggers an asymmetrical shift in the voltage phasors. Since the SEIG relies entirely on balanced reactive power to sustain its magnetising flux, any deficit in Phase C disrupts the equilibrium, forcing the generator to adjust its slip and shifting the operating point along the saturation curve to satisfy the reactive power balance equation ($Q_{\text{gen}} + Q_{\text{cap}} = 0$). This mechanism generates negative-sequence components and electromagnetic torque oscillations, which manifest

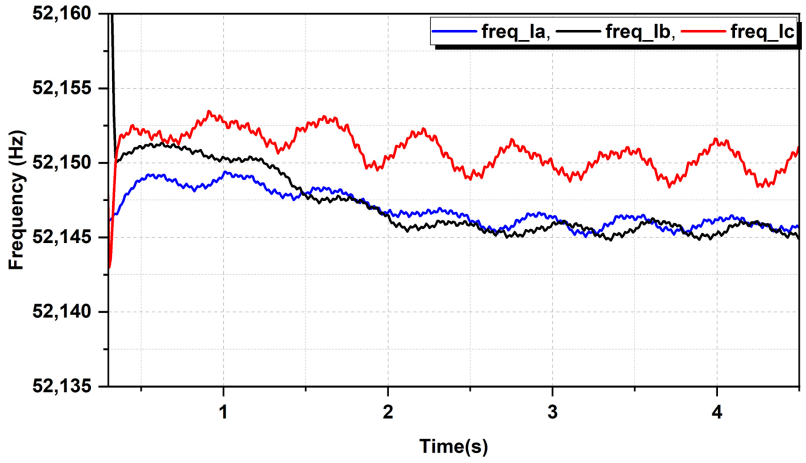

FIGURE 17. Estimated frequency of three-phase currents (I_a, I_b, I_c) for four capacitor failures.

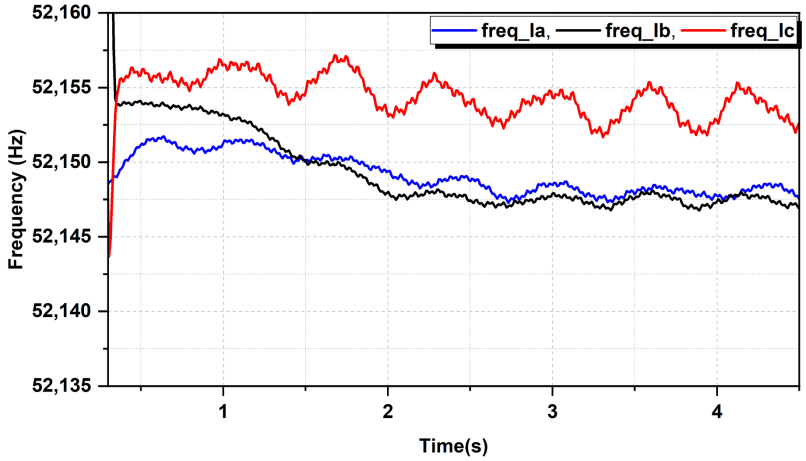

FIGURE 18. Estimated frequency of three-phase currents (I_a, I_b, I_c) for five capacitor failures.

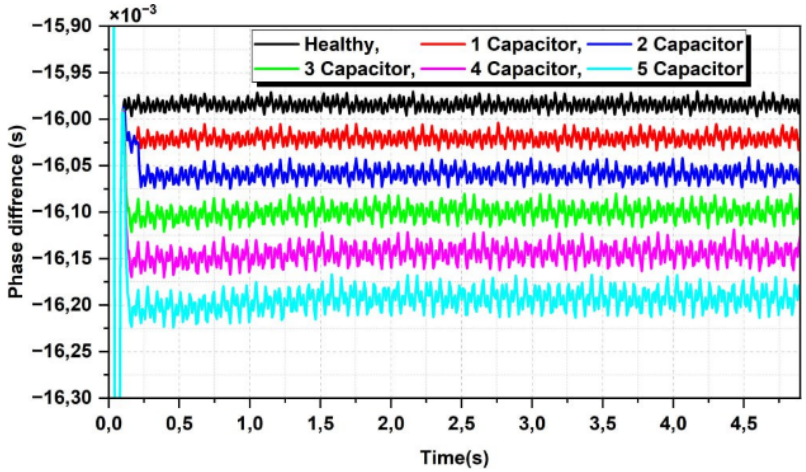

FIGURE 19. Phase differences between phase pair A-B.

as dynamic frequency fluctuations and distorted zero-crossing patterns, as can be seen in Figures 14–18. While the A-C pair (Figure 21) shows a systematic downward shift reaching -14.2×10^{-3}, these collective phase–frequency variations confirm a progressive misalignment associated with degradation.

From a practical standpoint, the distinct clusters observed in these phase-difference patterns can be utilised to develop a low-cost diagnostic firmware. By implementing these ZCT-based indicators into digital signal processors (DSPs), real-time protection systems can accurately distinguish between transient load fluctuations and early-stage capacitor degradation. This provides a computationally efficient solution for fault severity grading and predictive maintenance in off-grid wind energy systems, preventing critical failures.

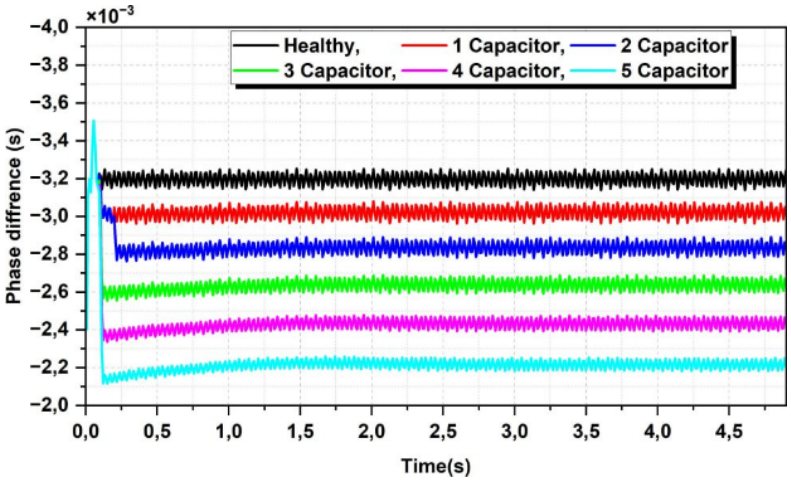

Figure 20. Phase differences between phase pair B-C.

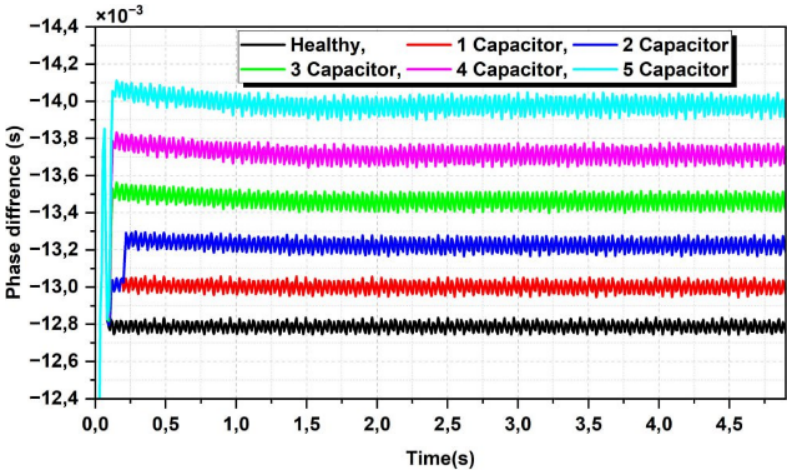

Figure 21. Phase differences between phase pair.

8. Conclusion

In this study, the behaviour of an SEIG was investigated under healthy conditions and progressive excitation capacitor faults using FEM simulations combined with ZCR analysis. The frequency of the generator remained tightly clustered between 52.135 Hz and 52.160 Hz, with a mean value of 52.14 Hz and a standard deviation of $\sigma < 0.005$. Progressive capacitor degradation, simulated by disconnecting one to five capacitors, introduced measurable distortions, with ZCR values varying between $100\,\mathrm{s}^{-1}$ and $110\,\mathrm{s}^{-1}$, indicating increasing instability in the electrical signals. During a steady operation, the frequency deviation remained below 0.02 Hz, whereas a fault condition was identified when the deviation exceeded 0.5 % of the nominal frequency. In addition, phase difference analysis of the phase pairs (A-B, B-C, and A-C) quantified the progressive asymmetry in the reactive power distribution resulting from capacitor degradation. The combined FEM simulation and ZCR-based measurements provide complementary information in the time and frequency domains and support the use of phase and frequency deviations as indicators for monitoring capacitor faults in off-grid wind-driven SEIG systems.

References

[1] M. J. B. Kabeyi, O. A. Olanrewaju. Sustainable energy transition for renewable and low carbon grid electricity generation and supply. *Frontiers in Energy Research* **9**:743114, 2022. https://doi.org/10.3389/fenrg.2021.743114

[2] A. Q. Al-Shetwi. Sustainable development of renewable energy integrated power sector: Trends, environmental impacts, and recent challenges. *Science of The Total Environment* **822**:153645, 2022. https://doi.org/10.1016/j.scitotenv.2022.153645

[3] G. K. Singh. Self-excited induction generator research – A survey. *Electric Power Systems Research* **69**(2–3):107–114, 2004. https://doi.org/10.1016/j.epsr.2003.08.004

[4] V. B. M. Krishna, V. Sandeep, S. S. Murthy, K. Yadlapati. Experimental investigation on performance comparison of self excited induction generator and permanent magnet synchronous generator for small scale renewable energy applications. *Renewable Energy* **195**:431–441, 2022. https://doi.org/10.1016/j.renene.2022.06.051

[5] A. Dilmi, A. Bouzida, N. Yassa, et al. Enhancing the reliability of self-excited induction generators used in wind energy microgrids through a hybrid

FEM-CNN-based fault diagnosis framework. *Journal of Renewable and Sustainable Energy* **18**(1):016306, 2026. https://doi.org/10.1063/5.0312967

[6] C. F. Wagner. Self-excitation of induction motors. *Electrical Engineering* **58**(2):47–51, 1939. https://doi.org/10.1109/ee.1939.6431777

[7] F. Belynda, R. Abdelli, A. Bouzida. Stator current signal crossing for fault diagnosis of self-excited induction generators. *Acta Polytechnica* **63**(5):293–304, 2023. https://doi.org/10.14311/ap.2023.63.0293

[8] S. P. Singh, S. K. Jain, J. Sharma. Voltage regulation optimization of compensated self-excited induction generator with dynamic load. *IEEE Transactions on Energy Conversion* **19**(4):724–732, 2004. https://doi.org/10.1109/tec.2004.827711

[9] A. Najafi, I. Iskender. Electromagnetic force investigation on distribution transformer under unbalanced faults based on time stepping finite element methods. *International Journal of Electrical Power & Energy Systems* **76**:147–155, 2016. https://doi.org/10.1016/j.ijepes.2015.09.020

[10] R. de Jesus Romero-Troncoso. Multirate signal processing to improve FFT-based analysis for detecting faults in induction motors. *IEEE Transactions on Industrial Informatics* **13**(3):1291–1300, 2017. https://doi.org/10.1109/tii.2016.2603968

[11] A. Kucuker, M. Bayrak. Detection of mechanical imbalances of induction motors with instantaneous power signature analysis. *Journal of Electrical Engineering and Technology* **8**(5):1116–1121, 2013. https://doi.org/10.5370/jeet.2013.8.5.1116

[12] A. Ukil, S. Chen, A. Andenna. Detection of stator short circuit faults in three-phase induction motors using motor current zero crossing instants. *Electric Power Systems Research* **81**(4):1036–1044, 2011. https://doi.org/10.1016/j.epsr.2010.12.003

[13] Z. Zou, M. Chen, C. Yang, et al. Fault diagnosis method for marine electric propulsion systems based on zero-crossing tacholess order tracking. *Journal of Marine Science and Engineering* **12**(11):1899, 2024. https://doi.org/10.3390/jmse12111899

[14] S. Joo, J. Choi, N. Kim, M. C. Lee. Zero-crossing rate method as an efficient tool for combustion instability diagnosis. *Experimental Thermal and Fluid Science* **123**:110340, 2021. https://doi.org/10.1016/j.expthermflusci.2020.110340

[15] M. Z. Ali, M. N. S. K. Shabbir, X. Liang, et al. Machine learning-based fault diagnosis for single- and multi-faults in induction motors using measured stator currents and vibration signals. *IEEE Transactions on Industry Applications* **55**(3):2378–2391, 2019. https://doi.org/10.1109/tia.2019.2895797

[16] J. Faiz, B. M. Ebrahimi, B. Akin, H. A. Toliyat. Finite-element transient analysis of induction motors under mixed eccentricity fault. *IEEE Transactions on Magnetics* **44**(1):66–74, 2008. https://doi.org/10.1109/tmag.2007.908479

[17] A. Bouzida, R. Abdelli, O. Touhami, et al. Dynamic eccentricity fault diagnosis in induction motors using finite element method and experimental tests. *International Journal of Industrial Electronics and Drives* **3**(4):199–209, 2017. https://doi.org/10.1504/ijied.2017.087610

[18] N. H. Malik, A. A. Mazi. Capacitance requirements for isolated self excited induction generators. *IEEE Transactions on Energy Conversion* **EC-2**(1):62–69, 1987. https://doi.org/10.1109/tec.1987.4765805

[19] A. K. Al Jabri, A. I. Alolah. Capacitance requirement for isolated self-exicted induction generator. *IEE Proceedings B (Electric Power Applications)* **137**(3):154–159, 1990. https://doi.org/10.1049/ip-b.1990.0016

[20] T. F. Chan. Capacitance requirements of self-excited induction generators. *IEEE Transactions on Energy Conversion* **8**(2):304–311, 1993. https://doi.org/10.1109/60.222721

[21] W. E. Vanco, F. B. Silva, F. A. S. Goncalves, C. A. Bissochi. Evaluation of the capacitor bank design for self-excitation in induction generators. *IEEE Latin America Transactions* **16**(2):482–488, 2018. https://doi.org/10.1109/tla.2018.8327403

[22] R. R. Shenoy, C. S. Seelamantula. Spectral zero-crossings: Localization properties and applications. *IEEE Transactions on Signal Processing* **63**(12):3177–3190, 2015. https://doi.org/10.1109/tsp.2015.2420538

[23] Q. Chen, T. Liu, X. Wu, H. Li. Modeling and optimization for fault diagnosis of electromechanical systems based on zero crossing algorithm. *Mathematical Problems in Engineering* **2020**:9267838, 2020. https://doi.org/10.1155/2020/9267838

[24] K. Maresch, L. F. Freitas-Gutierres, A. L. Oliveira, et al. Advanced diagnostic approach for high-voltage insulators: Analyzing partial discharges through zero-crossing rate and fundamental frequency estimation of acoustic raw data. *Energies* **16**(16):6033, 2023. https://doi.org/10.3390/en16166033

[25] R. C. Guido. ZCR-aided neurocomputing: A study with applications. *Knowledge-Based Systems* **105**:248–269, 2016. https://doi.org/10.1016/j.knosys.2016.05.011

[26] D. A. Ramli, N. Ghazali, L. Tay. Ischemic stroke detection system with computer aided diagnostic capability. *Procedia Computer Science* **126**:393–402, 2018. https://doi.org/10.1016/j.procs.2018.07.273

[27] B. Trajin, M. Chabert, J. Regnier, J. Faucher. Hilbert versus Concordia transform for three-phase machine stator current time-frequency monitoring. *Mechanical Systems and Signal Processing* **23**(8):2648–2657, 2009. https://doi.org/10.1016/j.ymssp.2009.05.015

[28] D. J. Gross, A. Matytsin. Instanton induced large N phase transitions in two- and four-dimensional QCD. *Nuclear Physics B* **429**(1):50–74, 1994. https://doi.org/10.1016/s0550-3213(94)80041-3

[29] B. Kedem. Search for periodicities by axis-crossings of filtered time series. *Signal Processing* **10**(2):129–144, 1986. https://doi.org/10.1016/0165-1684(86)90015-0